

High-throughput electro-optic upconversion and downconversion with few-photon added noise

M. D. Urmeý,^{1,2} S. Dickson,^{1,2} K. Adachi,^{1,2} S. Mittal,^{1,2} L. G. Talamo,^{1,2}
A. Kyle,^{1,2} N. E. Frattini,^{1,2} S.-X. Lin,^{1,2} K. W. Lehnert,³ and C. A. Regal^{1,2}

¹*JILA, National Institute of Standards and Technology and the University of Colorado, Boulder, Colorado, 80309, USA*

²*Department of Physics, University of Colorado, Boulder, Colorado, 80309, USA*

³*Department of Physics, Yale University, New Haven, Connecticut 06511, USA*

(Dated: July 15, 2025)

A microwave-optical transducer of sufficiently low noise and high signal transfer rate would allow entanglement to be distributed between superconducting quantum processors at a rate faster than the lifetimes of the quantum memories being linked. Here we present measurements of a membrane-based opto-electromechanical transducer with high signal throughput, as quantified by an efficiency-bandwidth-duty-cycle product of 7 kHz, approaching quantum-enabled operation in upconversion as well as downconversion, with input-referred added noise of 3 photons. In downconversion, throughput of this magnitude at the few-photon noise level is unprecedented. Using the quantum channel capacity, we also find an expression for the maximum rate at which quantum information can be transduced, providing insight into the importance of improving both a transducer's throughput and noise performance. With feasible improvements, the high throughput achieved with this device positions membrane-based transducers as a strategic choice for demonstrations of a quantum network with reasonable averaging times.

A transducer bridging microwave and optical frequencies with sufficiently low noise would allow the deterministic generation of arbitrary optical quantum states for applications in metrology, the storage and manipulation of optical quantum information, and the networking of remote superconducting quantum processors. Reducing input-referred added noise N_{add} to as low a level as possible is imperative for such quantum state manipulation. At the same time, it is useful to increase the rate of transduction to enable transducing signals at rates that are compatible with the lifetimes of logical qubits that process the transduced quantum information. Current state-of-the-art lifetimes in superconducting architectures are approximately 1 ms using physical qubits [1, 2], 1 ms using error-corrected bosonic encodings [3], and 300 μs using logical encodings of many physical qubits [4]. Finite qubit lifetimes place constraints not only on the transducer bandwidth B (which must be fast enough to transduce quantum information within the time qubits can faithfully store it), but also on the overall signal throughput in order to support an entangled bit rate much faster than decoherence rates. Signal throughput is further reduced by less-than-unity transducer efficiency η and duty cycle D , underscoring the importance of increasing the throughput of quantum transducers, even as progress is made on logical lifetimes of quantum memories. In practice, there is often a tradeoff between noise performance and throughput, as increasing throughput frequently involves increasing the average drive power, which can lead to heating-induced noise.

Concurrent with improving the performance of electro-optic transducers, a fully developed transducer platform would be capable of operating in both directions of frequency conversion. For instance, there are several pro-

posed protocols for sharing entanglement between separated quantum systems, and these place different demands on the transducers in a network of microwave-frequency nodes linked optically. Long-range quantum networks dominated by loss will likely benefit from using heralding protocols, in which entanglement infidelity due to inefficiency is mitigated at the cost of transmission rates and greater noise sensitivity [5]. Such a protocol favors a network topology with transducers operating in upconversion (from microwave to optical frequencies) to take advantage of mature optical single-photon-detection technologies [6]. On the other hand, transducers operating in downconversion (from optical to microwave frequencies) would be useful for generating entanglement from squeezed optical light [7]. Further, deterministic state transfer protocols [8, 9] are possible if efficiencies are high, and require one transducer operating in upconversion and one in downconversion. In general, a transducer's performance can be asymmetric between the two directions of frequency conversion, depending on the origin of the dominant source of noise. Published work to date has typically operated more favorably in upconversion than in downconversion, in the relatively few works where downconversion performance has been demonstrated and quantified [10, 11].

In this work, we present measurements of a transducer with high throughput, $\Theta = \eta BD$ exceeding 7 kHz, and noise performance close to input-referred added noise $N_{\text{add}} = 1$, expressed in units of photons, or photons per second per Hz of bandwidth, in upconversion ($N_{\text{add}}^{\text{up}} = 2.6$) as well as downconversion ($N_{\text{add}}^{\text{down}} = 3$). While similar throughputs have been achieved in a device with quantum-enabled performance in upconversion [12], in downconversion, our device increases throughput by

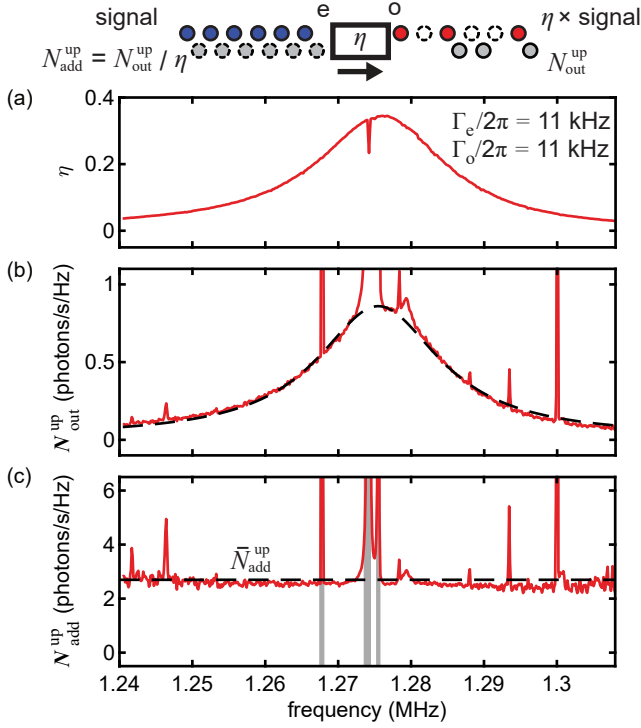


FIG. 1. Upconversion transducer performance with $B = 22$ kHz. The apparent efficiency η quantifies the fraction of the incident microwave signal (blue circles) that is transduced to optical frequencies (red circles), rather than lost (empty dashed circles). The upconversion input-referred added noise $N_{\text{add}}^{\text{up}}$ (gray dashed circles) compares the noise rate measured at the output $N_{\text{out}}^{\text{up}}$ (gray circles) to a potential signal at the input. (a) Apparent transduction efficiency η vs. signal detuning from pump $\omega/2\pi$. (b) Output-referred upconversion noise spectrum. (c) Input-referred added noise spectrum in upconversion. The grayed-out regions indicate frequency bands contaminated by noise from the high thermal occupation of optomechanically stiff modes. Excluding these regions and integrating the noise across the bandwidth of the transducer yields $\bar{N}_{\text{add}}^{\text{up}} = 2.7$ (horizontal dashed line).

three orders of magnitude over the leading quantum demonstration [11], at the cost of a single order of magnitude worse noise performance. Our platform achieves such performance due to its robustness to strong optical pumping, as demonstrated in previous work [13], as well as significant improvement to the electrical circuit that we show here.

As transducers push the boundaries of both lower noise and higher throughput, it is important to understand the impacts of each of these two parameters in quantum networks, beyond the requirement $N_{\text{add}} < 1$. We approach this analysis by mathematically integrating the quantum channel capacity, in the case of transducers with spectrally flat, thermal input-referred added noise, and find an expression that assesses transducer utility using noise and throughput.

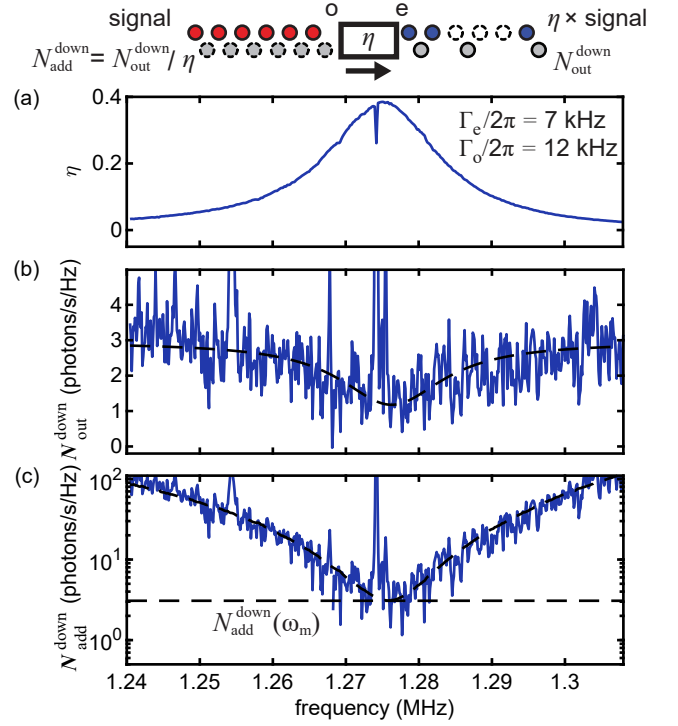


FIG. 2. Downconversion transducer performance with $B = 19$ kHz. (a) Apparent transduction efficiency η vs. signal detuning from pump $\omega/2\pi$. (b) Downconversion output-referred noise spectrum. The broadband noise contribution extending beyond the damped linewidth of the transduction mode is due to unwanted additional occupation of the LC circuit resulting from the microwave pump. Destructive interference between this microwave noise and the mechanical motion it drives results in noise squashing (Eq. 2). (c) Input-referred added noise spectrum in downconversion. Broadband circuit noise divided by the frequency-dependent η results in $N_{\text{add}}^{\text{down}}$ increasing with detuning from the center of the transduction bandwidth. Additionally, noise squashing near resonance suppresses the noise level near $\omega_m/2\pi = 1.27$ MHz.

Characterizing high-throughput performance

Our transducer is a doubly-parametric membrane-based transducer of similar design to Refs. [13, 14], with the following improvements: the silicon nitride Si_3N_4 in the device is annealed [15], and the membrane is “pinned” in place with a silicon post to more reproducibly set the transducer’s capacitor spacing [16, 17]. Furthermore, we have improved the noise performance of the optical and microwave pumps with additional filtering (Methods). The mechanical mode of the Si_3N_4 membrane with resonant frequency $\omega_m = 2\pi \cdot 1.27$ MHz couples an optical Fabry-Pérot cavity and a microwave-frequency superconducting LC circuit via the optomechanical and electromechanical interactions [18]. Electrical and optical pumps red-detuned by ω_m from their respective resonators enhance these interactions, coupling the mechanical mode to the microwave (optical) field at

rate Γ_e (Γ_o), proportional to the pump power. Imperfect suppression of the Stoke's sideband of the transduction mode leads to gain $\mathcal{A} = \mathcal{A}_e \mathcal{A}_o$, where \mathcal{A}_e (\mathcal{A}_o) is the portion of the gain due to the electromechanical (optomechanical) interaction, which is undesirable because it is accompanied by additional noise [18, 19]. The apparent efficiency $\eta = \mathcal{A}\eta_t$ includes this gain factor and gives the fraction of the incident signal that exits the transducer, where $\eta_t = \eta_M(4\Gamma_e\Gamma_o/\Gamma_T^2)$ is the ideal transduction efficiency of a device operating with perfect optomechanical and electromechanical sideband resolution [13], and the maximum achievable efficiency η_M is limited by loss in the electromagnetic resonators and an optical mode matching factor. Our platform achieves the highest external microwave-optical transduction efficiencies demonstrated to date [13]. In this device we achieve apparent efficiencies of $\eta = 0.4$, calibrated by the procedure used in Ref. [20]. The transduction bandwidth $B = \Gamma_T/2\pi$ is determined by the total loss rate of the mechanical mode, including the pump-enhanced loss rates, $\Gamma_T = \Gamma_e + \Gamma_o + \gamma_m$, where $\gamma_m \ll \Gamma_e, \Gamma_o$ is the intrinsic loss rate of the transduction mode.

The measured bidirectional apparent efficiency $\eta(\omega) = \sqrt{\epsilon_{PL}} |S_{eo}(\omega)| |S_{oe}(\omega)| / |S_{ee}(\omega)| |S_{oo}(\omega)|$ is shown in Fig. 1(a), where e.g. S_{oe} denotes the scattering parameter governing a signal incident on the port electrical port “e” and detected from the optical port “o”, and ϵ_{PL} is a factor quantifying the spatial mode matching of the optical pump and local oscillator beam used for heterodyne readout [18]. The efficiency follows a Lorentzian lineshape corresponding to the susceptibility of the damped mechanical transduction mode. In addition to the optomechanically compliant mode that we use for transduction, our device also exhibits optomechanically stiff modes, characterized by significant motion in the massive substrate that makes them resistant to optomechanical damping. The dip in the efficiency at frequency $\omega_s/2\pi = 1.275$ MHz and approximate width of 1 kHz in Fig. 1(a) is due to one such mode, and is the result of destructive interference of the coherent signal tone propagating through both the stiff mode and the compliant mode. The prominence of stiff modes in this generation of device is due to an error in the fabrication geometry, which can be addressed in subsequent designs (Methods).

The output-referred noise spectrum $N_{out}^{up} = N_{det,o}/\xi_o$ (Fig. 1(b)) corresponds to the noise measured at the optical heterodyne detection $N_{det,o}$ in units of photons/s/Hz, divided by the total detection efficiency ξ_o between the output of the transducer and the detected voltage (see Ref. [13] for additional details). Here we measure ξ_o by calibrating the optomechanically measured spectrum in phonon units using sideband asymmetry thermometry. In addition to the thermomechanical noise following the Lorentzian profile of the damped compliant mode, the spectrum shows structure due to multiple stiff modes

whose large thermally driven motion is written onto the optically measured output spectrum. The Lorentzian fit (dashed curve) excludes the stiff modes, to provide a guide to the eye. The fit departs from the measurement in the tails because of a small asymmetry in the spectrum due to interference with a highly damped membrane mode with a 950 kHz resonant frequency.

Whereas previous work has focused on the noise level at the center of the transduction bandwidth, in order to more transparently assess the potential of transducing a signal, we compute the frequency-dependent input-referred added noise N_{add}^{up} (Fig. 1(c)) by referring the optical output spectrum shown in Fig. 1(b) to the input of the device by dividing by an interpolation of the frequency-dependent transduction efficiency in Fig. 1(a): $N_{add}^{up}(\omega) = N_{out}^{up}(\omega)/\eta(\omega)$. Neglecting the features due to the stiff modes, the N_{add}^{up} spectrum is relatively flat over the frequency band relevant for the transducer. Notching out the frequencies corresponding to the grey regions in Fig. 1(c) and integrating the total contributed noise, we obtain an average added noise of $\bar{N}_{add}^{up} = 2.7(3)$ over the bandwidth of the transducer (Methods), close to the value of the input referred added noise at the transducer's maximum efficiency, as determined by the fit to the noise peak, $N_{add}^{up}(\omega_m) = 2.6(3)$. The uncertainty in both \bar{N}_{add}^{up} and $N_{add}^{up}(\omega_m)$ is dominated by the statistical uncertainty of the fit parameters in the sideband asymmetry thermometry measurement used to extract ξ_o and calibrate this $N_{add}^{up}(\omega)$ spectrum. If we were to physically implement such a sharp filter in a quantum network, the ringing of the narrow filter would only modestly impact the throughput and noise performance (Methods). Depending on the application, shaping the signal pulses to avoid problematic frequency regions or using a selective demodulation envelope in detection are also viable solutions to such frequency-dependent noise profiles. Of course, the more practical solution to the additional noise of the stiff modes is to eliminate them altogether.

The operating parameters used in Fig. 1 achieve $B = 22$ kHz, which represent an improvement in bandwidth by approximately two orders of magnitude compared with the device measured in Ref. [13]. Though it may be expected that such an increase in optomechanical and electromechanical damping rates would come at the cost of a commensurate increase in the noise, we measure similar baseline noise levels, i.e. neglecting the noise caused by the stiff modes. This improvement in the robustness of our transducer to strong driving is due to improvement of the single-photon electromechanical coupling rate g_e , reduction in phase noise of both optical and microwave pumps from additional filtering (Methods), and annealing the Si_3N_4 to remove two-level-system defects [15] that were a source of internal loss and, as we find here (Methods), noise in the microwave circuit.

Fig. 2 shows downconversion measurements analogous to those in Fig. 1. Unlike in upconversion, wideband

noise extends beyond the bandwidth of the transduction mode due to occupation of the microwave resonator (Fig. 2(b)). This additional noise is associated only with driving the circuit strongly with the microwave pump; we do not observe additional occupation associated with the strong optical pump. Because the microwave noise field also drives the mechanical mode, there is interferometric cancellation at the mechanical frequency leading to squashing measured at the output port [21, 22]. The deficit of noise seen at this output is instead routed out the optical port optomechanically. In Fig. 2(c), in addition to $N_{\text{add}}^{\text{down}}$ being suppressed from squashing near mechanical resonance, $N_{\text{add}}^{\text{down}}$ increases with further detuning from the transduction mode because the relatively broadband noise from microwave circuit occupation is divided by the frequency-dependent conversion efficiency. Unlike upconversion performance, the $N_{\text{add}}^{\text{down}}(\omega)$ spectrum is frequency dependent, and the impact of the off-resonant noise would depend on the details of the network the transducer is embedded in and the protocol used. We therefore for simplicity report downconversion performance using the noise at peak efficiency $N_{\text{add}}^{\text{down}}(\omega_m)$ (horizontal dashed line), determined from the minimum of the fit to $N_{\text{out}}^{\text{down}}(\omega)$ referred to the optical input (dashed curve), in line with previous work [13, 20, 23], and analogous to applying additional filtering on $N_{\text{out}}^{\text{down}}$ [10]. The increase in statistical noise in the spectrum measurements shown in Fig. 2 relative to those in Fig. 1 is due to the difference between the optical measurement efficiency $\xi_o = 0.4$ and the measurement efficiency of the HEMT amplifier and microwave detection chain $\xi_e = 0.01$. The reduced signal-to-noise ratio made calibrating ξ_e electromechanically via sideband asymmetry impractical, so instead we took advantage of our simultaneous optomechanical and electromechanical measurement of the prominent stiff modes (Methods).

Contributions to added noise

To explore noise performance and its differences in upconversion and downconversion, we distinguish expressions for $N_{\text{add}}^{\text{up}}(\omega_m)$ and $N_{\text{add}}^{\text{down}}(\omega_m)$, making the simplifying assumptions of lossless cavities operating in the resolved sideband regime $\kappa_e, \kappa_o \ll 4\omega_m$ with perfect optical mode matching:

$$N_{\text{add}}^{\text{up}}(\omega_m) = \underbrace{\frac{n_{\text{th}}\gamma_m}{\Gamma_e} + n_{\text{em}} + \frac{n_{\text{om}}\Gamma_o}{\Gamma_e}}_{N_{\text{add},m}} + \underbrace{\frac{\bar{n}_o\Gamma_T^2}{\Gamma_e\Gamma_o}}_{N_{\text{add},e/o}} - \underbrace{\frac{2\bar{n}_o\Gamma_T}{\Gamma_e}}_{N_{\text{add},\text{corr}}} \quad (1)$$

and

$$N_{\text{add}}^{\text{down}}(\omega_m) = \underbrace{\frac{n_{\text{th}}\gamma_m}{\Gamma_o} + n_{\text{om}} + \frac{n_{\text{em}}\Gamma_e}{\Gamma_o}}_{N_{\text{add},m}} + \underbrace{\frac{\bar{n}_e\Gamma_T^2}{\Gamma_o\Gamma_e}}_{N_{\text{add},e/o}} - \underbrace{\frac{2\bar{n}_e\Gamma_T}{\Gamma_o}}_{N_{\text{add},\text{corr}}} \quad (2)$$

where n_{th} is the environmental mechanical occupation, \bar{n}_o is the effective occupation of the optical cavity due to thermal occupation or the presence of technical noise on the optical pump, and $n_{\text{om}} = \bar{n}_o + n_{\text{min},o}$ is the bath occupation that the mechanical mode is coupled to optomechanically, with $n_{\text{min},o}$ denoting the optomechanical backaction limit [24]. The quantities associated with the electrical port n_{em} , \bar{n}_e , and $n_{\text{min},e}$ are defined analogously. In the resolved-sideband limit, $n_{\text{om}} = \bar{n}_o$, but we differentiate these noise contributions explicitly here to clarify their physical origins. In Eqs. 1 and 2, the first three terms comprise noise from motion of the transduction mode $N_{\text{add},m}$, and the fourth term $N_{\text{add},e/o}$ is from noise purely of electromagnetic origin measured at the output port. The fifth term $N_{\text{add},\text{corr}}$ results from destructive interference between the fields responsible for the third and fourth terms.

Noise performance between upconversion and downconversion can be asymmetric. In the limit $\Gamma_o = \Gamma_e$, the impedance matching criterion that achieves unit efficiency, Eqs. 1 and 2 become the same (for lossless cavities), even in the presence of additional electromagnetic noise at the output port. However, when n_{em} , n_{om} , and n_{th} differ, often better performance in one direction can be achieved by mismatching the pump strengths. Practically, the most significant physical effect causing asymmetric transducer performance is that occupations are in general pump-power dependent quantities, and therefore can depend on Γ_e and Γ_o :

$$n_{\text{th}}(\Gamma_e, \Gamma_o); \bar{n}_e(\Gamma_e, \Gamma_o); \bar{n}_o(\Gamma_e, \Gamma_o). \quad (3)$$

In particular, transduction experiments have observed occupations of the form $n_{\text{th}}(\Gamma_o)$ [11, 12], $\bar{n}_e(\Gamma_e)$ [13], or $\bar{n}_e(\Gamma_o)$ [11]. Terms of the form $\bar{n}_e(\Gamma_o)$ or $n_{\text{th}}(\Gamma_o)$ are common because of the high energy of optical photons compared with the lower frequency scales of the microwave and mechanical excitations used in transducers, and are ruinous for downconversion performance at high optical power and high duty cycle. Though Eqs. 1 and 2 apply specifically to doubly-parametric transducers [12, 13], the noise in other architectures also depends on the transducer's thermal environment and coupling rates, and similar expressions can be written. The fact that our membrane-based platform does not exhibit noise terms proportional to Γ_o is the reason for its downconversion noise performance, even though we operate it with high optical circulating powers of approximately 3 mW in this work.

In upconversion, because of its low optical noise and sufficient sideband resolution, our transducer's noise performance is determined by the first two terms in Eq. 1 (i.e. $n_{\text{th}}\gamma_m/\Gamma_e + n_{\text{em}}$), as long as Γ_e and Γ_o are reasonably well-matched. Notably, this approximation implies that $N_{\text{add}}^{\text{up}}$ is independent of Γ_o . As we observe the microwave circuit occupation to follow the form $\bar{n}_e = a_e\Gamma_e + b_e$ [13] (Methods), the contributions to $N_{\text{add}}^{\text{up}}$ consist of a component of thermomechanical origin that scales as $1/\Gamma_e$, and a component due to LC circuit occupation that increases linearly with Γ_e . Optimal noise performance in upconversion is achieved by tuning Γ_e to balance these two contributions (see Fig. 3(a) below).

Turning to downconversion performance, the first three terms of Eq. 2 reveal that, in striking contrast with upconversion, $N_{\text{add,m}}$ can be made quite small simply by increasing Γ_o , because the excess motional noise can be routed out the input port by increasing the low-noise optical pump.

If motion of the membrane were the only source of noise, like it is in upconversion, our device would demonstrate quite asymmetrical performance, favoring operation in downconversion with large Γ_o . However, when our device operates in downconversion, the microwave field also contributes to N_{add} through $N_{\text{add,e/o}}$. Assuming $\Gamma_T = \Gamma_o + \Gamma_e$ to combine the last three terms of Eq. 2, we have

$$N_{\text{add}}^{\text{down}}(\omega_m) = \frac{n_{\text{th}}\gamma_m}{\Gamma_o} + n_{\text{om}} + \frac{\bar{n}_e\Gamma_o}{\Gamma_e} + \frac{n_{\text{min,e}}\Gamma_e}{\Gamma_o}. \quad (4)$$

Again parameterizing $\bar{n}_e = a_e\Gamma_e + b_e$ as above, $N_{\text{add}}^{\text{down}}$ contains terms proportional to Γ_o and Γ_o/Γ_e , so occupation of the microwave circuit prevents arbitrary improvement in downconversion performance with increasing Γ_o . Additionally, the last term in Eq. 4 indicates that finite sideband resolution contributing to nonzero $n_{\text{min,e}}$ limits the ratio Γ_e/Γ_o , causing increased noise at high microwave drive strength. Optimal downconversion performance is then achieved by tuning Γ_o to balance $n_{\text{th}}\gamma_m$ against a_e , and Γ_e/Γ_o to balance $n_{\text{min,e}}$ against b_e (see Fig. 3(b) below).

Noise and throughput in transducers

In general, there is a trade-off between the added noise of a transducer, and the rate of successful signal transmission as determined by the transduction efficiency and bandwidth. In platforms that pulse their operation to avoid additional unwanted noise, the reduced duty cycle can further limit this communication rate. Here, we identify a transducer's throughput Θ [12, 13] quantitatively with the efficiency-bandwidth-duty-cycle product $\Theta = \eta BD$, as a way to characterize the total rate of a transducer. Roughly, it gives the expected rate that sin-

gle photon signals are detected at the output of a transducer, when sent at a repetition rate of B .

To experimentally demonstrate the competition between throughput and noise in our device, in Figs. 3(a) and (b) we display results of varying Γ_e while holding Γ_o roughly fixed at $\Gamma_o = 2\pi \cdot 11$ kHz, and quantify $N_{\text{add}}(\omega_m)$ and Θ . The data points corresponding to the measurements shown in Figs. 1 and 2 are marked with hearts. The black lines show the predicted performance of our transducer using independently calibrated measurements and modified versions of Eqs. 1 and 2 that account for lossy cavities and finite sideband resolution (Methods). These model curves illustrate the turnaround expected by increasing the throughput (by increasing Γ_e) from inspecting Eqs. 1 and 2. In upconversion, we see agreement between this model and our measurements, and in downconversion, we see qualitative agreement that reproduces the general trend of our measurement.

In Figs. 3(c) and (d), we put the respective performance measurements in upconversion and downconversion in the context of other results in the field, using a format similar to that first used in Ref. [12]. We see that the throughputs we achieve at the noise levels we measure are consistent with the best achieved in the field in upconversion, although unlike the device in Ref. [12], the turnaround due to thermomechanical motion at low throughputs prevents our current device from achieving quantum operation. Relative to our previous work [13], this turnaround occurs at higher throughput because of a γ_m that is over an order-of-magnitude higher, as measured electromechanically by ringdown of the transduction mode. In downconversion, our platform achieves over three orders of magnitude higher throughput, at the cost of one order of magnitude increase in N_{add} , compared with the leading downconversion demonstration in the field [11].

A rate for quantum transduction

For practical applications of a quantum transducer, improvements to both noise and throughput performance are needed in the field, and both metrics are important for the overall quantum information transfer rate. For example, a noisy quantum channel may necessitate the use of entanglement distillation protocols, consuming some quantity of low-fidelity entanglement in order to produce fewer entangled pairs of higher fidelity [30, 31]. A higher-throughput transducer would better enable distillation protocols by making a greater quantity of entangled pairs available within the lifetime of the quantum memories, while a lower-throughput and lower-noise transducer may be able to achieve a comparable total rate.

A channel's quantum capacity gives the theoretical limit to the rate at which quantum information may be transmitted through it, and is therefore a possible met-

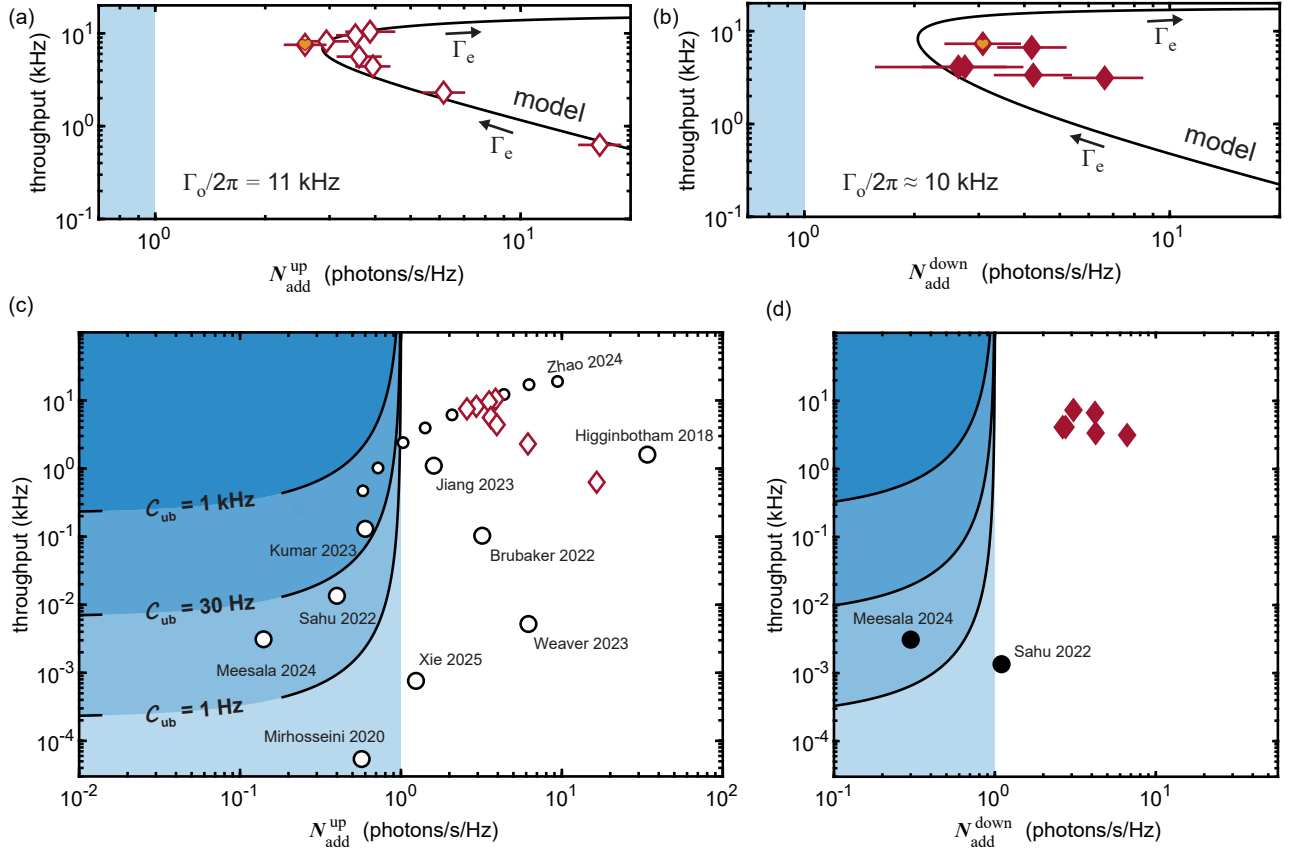


FIG. 3. Transducer performance. Device performance in upconversion (a) and downconversion (b). Maroon diamonds are measurements of our transducer taken while sweeping Γ_e with fixed $\Gamma_o = 2\pi \cdot 11$ kHz in (a), and $\Gamma_o/2\pi$ roughly fixed in (b), in the range 9–12 kHz. Inconsistency in Γ_o in (b) is due to drifts in the mode matching between the optical pump and the transducer optical cavity over the longer averaging times required for downconversion spectrum measurements. Error bars indicate one standard deviation, and are dominated by statistical uncertainty in the fit parameters used to infer the measurement efficiency. Error bars in the y -direction are smaller than the data points. The black line is performance modeled using independently measured parameters. Transducers have nonzero quantum capacity for $N_{\text{add}} < 1$ (light blue region). The quantum capacity of transducers in upconversion (c) and downconversion (d). Measurements presented in this work (maroon diamonds) are compared with other reported results (circles, labeled by first author)[10–13, 20, 25–29]. The high throughput measured in downconversion in this work is enabled by our platform’s robustness to optical circulating power. Contours indicate \mathcal{C}_{ub} as a function of a transducers throughput and N_{add} , assuming $\eta \ll 1$ and frequency-independent $N_{\text{add}}(\omega)$.

ric to use in evaluating a transducer’s performance. In the context of general-capability quantum nodes linked by noisy and lossy channels, using local operations and classical communication (LOCC) to process transmitted quantum information (e.g. using a heralding protocol) is likely important, as they are necessary for recovering nonzero rates when losses exceed 50% and one-way deterministic state transfer becomes impossible [32]. When LOCC operations are allowed, the upper bound to the rate is referred to as the two-way classically assisted quantum capacity \mathcal{c} , which quantifies the ability of the channel to transmit one qubit of information, or distribute one ebit of entanglement, on average per attempted use of the channel [33, 34].

To calculate a rate of quantum information transfer possible for a realistic channel with added noise, limited

efficiency, and finite bandwidth, we can integrate known upper bounds \mathcal{c}_{ub} on the quantum capacity \mathcal{c} for the thermal loss channel [34, 35], yielding an integrated capacity upper bound $\mathcal{C}_{\text{ub}} = \int \mathcal{c}_{\text{ub}} d\omega$. Assuming a frequency-independent N_{add} , which applies to our device’s operation in upconversion, we find that \mathcal{C}_{ub} is approximately linear in the throughput Θ for small efficiencies, and is given by

$$\mathcal{C}_{\text{ub}}(N_{\text{add}}, \Theta) \approx \frac{\pi \Theta}{\ln(2)} (1 - N_{\text{add}} + N_{\text{add}} \ln(N_{\text{add}})), \quad (5)$$

for $N_{\text{add}} < 1$ (see Methods for derivation). Though this approximation is pessimistic for channels with high efficiency, it remains accurate to within 17% for $\eta = 0.5$, and to within 3% for $\eta = 0.1$.

In the small- η limit, that \mathcal{C}_{ub} depends only on Θ and N_{add} gives theoretical motivation to the choice of axes to

summarize device performance in Ref. [12], and in Fig. 3. (For clarity, we here point out that, for example, the viability of deterministic state transfer protocols, which benefit from high efficiency, is not captured by Θ alone.) We can therefore overlay contours of C_{ub} onto Figs. 3(c) and (d), and gain an intuition for the relative importance of throughput and added noise in the quantum-enabled regime of $N_{add} < 1$. The contours make it apparent that although reducing N_{add} gives very sharp improvement while $N_{add} \approx 1$, further reductions in noise yield diminishing returns. Meanwhile, as C_{ub} is linear in B and D , and at least linear in η , improving a channel's throughput is always beneficial.

Conclusions

Reasonable improvements to our device design would allow quantum-enabled noise performance. Refinement of the engineered mechanical isolation of our pinned membrane would suppress the stiff modes in the mechanical spectrum and address the elevated mechanical intrinsic loss rate measured in this device (Methods). Recovering the mechanical coherence we have measured in previous generations of this device, combined with parallel improvement to the electromechanical design to increase the electromechanical coupling rate [36], would yield high-throughput quantum-enabled performance in both upconversion and downconversion. With transduction demonstrations improving in both throughput and added noise, we are rapidly approaching transducer integrated quantum capacities at the kHz-scale, at which point transducers would support, on average, the entanglement of one pair of superconducting qubits within every 1 ms physical lifetime.

-
- [1] S. Ganjam, Y. Wang, Y. Lu, A. Banerjee, C. U. Lei, L. Krayzman, K. Kisslinger, C. Zhou, R. Li, Y. Jia, *et al.*, Surpassing millisecond coherence in on chip superconducting quantum memories by optimizing materials and circuit design, *Nature Communications* **15**, 3687 (2024).
 - [2] M. P. Bland, F. Bahrami, J. G. Martinez, P. H. Prestegard, B. M. Smitham, A. Joshi, E. Hedrick, A. Pakpour-Tabrizi, S. Kumar, A. Jindal, *et al.*, 2d transmons with lifetimes and coherence times exceeding 1 millisecond, *arXiv preprint arXiv:2503.14798* (2025).
 - [3] V. V. Sivak, A. Eickbusch, B. Royer, S. Singh, I. Tsioutsios, S. Ganjam, A. Miano, B. Brock, A. Ding, L. Frunzio, *et al.*, Real-time quantum error correction beyond break-even, *Nature* **616**, 50 (2023).
 - [4] Suppressing quantum errors by scaling a surface code logical qubit, *Nature* **614**, 676 (2023).
 - [5] E. Zeuthen, A. Schliesser, A. S. Sørensen, and J. M. Taylor, Figures of merit for quantum transducers, *Quantum Science and Technology* **5**, 034009 (2020).
 - [6] F. Marsili, V. B. Verma, J. A. Stern, S. Harrington, A. E. Lita, T. Gerrits, I. Vayshenker, B. Baek, M. D. Shaw, R. P. Mirin, *et al.*, Detecting single infrared photons with 93% system efficiency, *Nature Photonics* **7**, 210 (2013).
 - [7] A. Kyle, C. L. Rau, W. D. Warfield, A. Kwiatkowski, J. D. Teufel, K. W. Lehnert, and T. Dennis, Optically distributing remote two-node microwave entanglement using doubly parametric quantum transducers, *Physical Review Applied* **20**, 014005 (2023).
 - [8] J. I. Cirac, P. Zoller, H. J. Kimble, and H. Mabuchi, Quantum state transfer and entanglement distribution among distant nodes in a quantum network, *Physical Review Letters* **78**, 3221 (1997).
 - [9] C. J. Axline, L. D. Burkhardt, W. Pfaff, M. Zhang, K. Chou, P. Campagne-Ibarcq, P. Reinhold, L. Frunzio, S. Girvin, L. Jiang, *et al.*, On-demand quantum state transfer and entanglement between remote microwave cavity memories, *Nature Physics* **14**, 705 (2018).
 - [10] R. Sahu, W. Hease, A. Rueda, G. Arnold, L. Qiu, and J. M. Fink, Quantum-enabled operation of a microwave-optical interface, *Nature communications* **13**, 1276 (2022).
 - [11] S. Meesala, S. Wood, D. Lake, P. Chiappina, C. Zhong, A. D. Beyer, M. D. Shaw, L. Jiang, and O. Painter, Non-classical microwave-optical photon pair generation with a chip-scale transducer, *Nature Physics* **20**, 871 (2024).
 - [12] H. Zhao, W. D. Chen, A. Kejriwal, and M. Mirhosseini, Quantum-enabled continuous microwave-to-optics frequency conversion, *arXiv preprint arXiv:2406.02704* (2024).
 - [13] B. M. Brubaker, J. M. Kindem, M. D. Urmey, S. Mittal, R. D. Delaney, P. S. Burns, M. R. Vissers, K. W. Lehnert, and C. A. Regal, Optomechanical ground-state cooling in a continuous and efficient electro-optic transducer, *Physical Review X* **12**, 021062 (2022).
 - [14] M. D. Urmey, S. Mittal, K. Adachi, L. G. Talamo, S. Dickson, S.-X. Lin, R. D. Delaney, B. M. Brubaker, J. M. Kindem, N. E. Frattini, *et al.*, Stable optomechanical fabry-pérot architecture in a continuous microwave-to-optical transducer, in *Quantum Computing, Communication, and Simulation IV*, Vol. 12911 (SPIE, 2024) pp. 82–91.
 - [15] S. Mittal, K. Adachi, N. E. Frattini, M. D. Urmey, S.-X. Lin, A. L. Emser, C. Metzger, L. Talamo, S. Dickson, D. Carlson, *et al.*, Annealing reduces Si_3N_4 microwave-frequency dielectric loss in superconducting resonators, *Physical Review Applied* **21**, 054044 (2024).
 - [16] M. D. Urmey, *Quantum Optomechanics With a Stable Fabry-Pérot Cavity in a Microwave-to-Optical Transducer*, Ph.D. thesis, University of Colorado at Boulder (2024).
 - [17] S. Mittal, *Enhanced Cooperativity in a Near-Quantum Microwave-to-Optical Transducer*, Ph.D. thesis, University of Colorado at Boulder (2024).
 - [18] R. W. Andrews, R. W. Peterson, T. P. Purdy, K. Cicak, R. W. Simmonds, C. A. Regal, and K. W. Lehnert, Bidirectional and efficient conversion between microwave and optical light, *Nature physics* **10**, 321 (2014).
 - [19] C. M. Caves, Quantum limits on noise in linear amplifiers, *Physical Review D* **26**, 1817 (1982).
 - [20] A. P. Higginbotham, P. Burns, M. Urmey, R. Peterson, N. Kampel, B. Brubaker, G. Smith, K. Lehnert, and C. Regal, Harnessing electro-optic correlations in an efficient mechanical converter, *Nature Physics* **14**, 1038

- (2018).
- [21] A. Jayich, J. Sankey, K. Børkje, D. Lee, C. Yang, M. Underwood, L. Childress, A. Petrenko, S. Girvin, and J. Harris, Cryogenic optomechanics with a si_3n_4 membrane and classical laser noise, *New Journal of Physics* **14**, 115018 (2012).
 - [22] A. H. Safavi-Naeini, J. Chan, J. T. Hill, S. Gröblacher, H. Miao, Y. Chen, M. Aspelmeyer, and O. Painter, Laser noise in cavity-optomechanical cooling and thermometry, *New Journal of Physics* **15**, 035007 (2013).
 - [23] W. Hease, A. Rueda, R. Sahu, M. Wulf, G. Arnold, H. G. Schwefel, and J. M. Fink, Bidirectional electro-optic wavelength conversion in the quantum ground state, *PRX Quantum* **1**, 020315 (2020).
 - [24] R. Peterson, T. Purdy, N. Kampel, R. Andrews, P.-L. Yu, K. Lehnert, and C. Regal, Laser cooling of a micromechanical membrane to the quantum backaction limit, *Physical review letters* **116**, 063601 (2016).
 - [25] M. Mirhosseini, A. Sipahigil, M. Kalaei, and O. Painter, Superconducting qubit to optical photon transduction, *Nature* **588**, 599 (2020).
 - [26] A. Kumar, A. Suleymanzade, M. Stone, L. Taneja, A. Anferov, D. I. Schuster, and J. Simon, Quantum-enabled millimetre wave to optical transduction using neutral atoms, *Nature* **615**, 614 (2023).
 - [27] T. Xie, R. Fukumori, J. Li, and A. Faraon, Scalable microwave-to-optical transducers at the single-photon level with spins, *Nature Physics* **21**, 931 (2025).
 - [28] M. J. Weaver, P. Duivesteyn, A. C. Bernasconi, S. Scharmer, M. Lemang, T. C. v. Thiel, F. Hijazi, B. Hensen, S. Gröblacher, and R. Stockill, An integrated microwave-to-optics interface for scalable quantum computing, *Nature nanotechnology* **19**, 166 (2024).
 - [29] W. Jiang, F. M. Mayor, S. Malik, R. Van Laer, T. P. McKenna, R. N. Patel, J. D. Witmer, and A. H. Safavi-Naeini, Optically heralded microwave photon addition, *Nature Physics* **19**, 1423 (2023).
 - [30] L.-M. Duan, G. Giedke, J. I. Cirac, and P. Zoller, Entanglement purification of gaussian continuous variable quantum states, *Physical Review Letters* **84**, 4002 (2000).
 - [31] F. A. Mele, L. Lami, and V. Giovannetti, Maximum tolerable excess noise in continuous-variable quantum key distribution and improved lower bound on two-way capacities, *Nature Photonics* **19**, 329 (2025).
 - [32] M. M. Wolf, D. Pérez-García, and G. Giedke, Quantum capacities of bosonic channels, *Physical review letters* **98**, 130501 (2007).
 - [33] C. H. Bennett, D. P. DiVincenzo, and J. A. Smolin, Capacities of quantum erasure channels, *Physical Review Letters* **78**, 3217 (1997).
 - [34] S. Pirandola, R. Laurenza, C. Ottaviani, and L. Banchi, Fundamental limits of repeaterless quantum communications, *Nature communications* **8**, 15043 (2017).
 - [35] C.-H. Wang, F. Li, and L. Jiang, Quantum capacities of transducers, *Nature Communications* **13**, 6698 (2022).
 - [36] A. Youssefi, S. Kono, M. Chegnizadeh, and T. J. Kippenberg, A squeezed mechanical oscillator with millisecond quantum decoherence, *Nature Physics* **19**, 1697 (2023).
 - [37] J. D. Teufel, T. Donner, D. Li, J. W. Harlow, M. Allman, K. Cicak, A. J. Sirois, J. D. Whittaker, K. W. Lehnert, and R. W. Simmonds, Sideband cooling of micromechanical motion to the quantum ground state, *Nature* **475**, 359 (2011).
 - [38] W. Jiang, D. Xu, S. Yao, B. Xiong, and Y. Wang, Effect of hyperthermal annealing on lpcvd silicon nitride, *Materials Science in Semiconductor Processing* **43**, 222 (2016).

METHODS

Technical noise

Though ground-state cooling the mechanical mode of our transducer has required low-noise optical and microwave pumps [13], in this work we further suppress technical noise by increasing the filtering of both the optical and microwave pumps in order to reach increased transduction bandwidths.

We introduce an additional 130 kHz-linewidth filter cavity to the optical setup detailed in Ref. [13], to filter the output of our Toptica CTL 1050 source laser. The remainder of the beam preparation remains as previously described [13]: the output of the 130 kHz filter cavity seeds a fiber amplifier, whose output is filtered by a second, 80 kHz-linewidth, filter cavity, and the beam then passes through a double-pass acousto-optic modulator (AOM) before being split to generate the locking, local oscillator, and optical pump beams. Using Pound-Drever-Hall locking, the beam is stabilized to the transducer's optical cavity by feeding back to the double-pass AOM and to a piezo on one mirror of the 80 kHz filter cavity. Two additional PDH feedback loops lock the frequency of the laser to that of the 130 kHz filter cavity, and the frequency of the 130 kHz cavity frequency to that of the 80 kHz filter cavity by actuating a piezo on the 130 kHz filter cavity. We measure no increase in noise due to the fiber amplifier on the light that is filtered by the 130 kHz cavity. The additional optical filtering, combined with improved electrical filtering of RF signals used in beam preparation, reduces the phase noise of the optical pump incident on the transducer at a detuning of ω_m to -155 dBc/Hz [16], allowing operation of our transducer at ~ 10 kHz optical dampings with negligible optical contribution to total noise.

The effective occupation of the microwave circuit \bar{n}_e , can have significant contributions from microwave generator phase noise and additional thermal occupation of the circuit, both of which scale with Γ_e [13]. In this work, we render the contribution from microwave generator phase noise to be negligible using a room temperature microwave-frequency cavity to filter out the generator phase noise that is on resonance with our LC circuit [37]. We use a high- Q mode of a cylindrical copper cavity whose frequency is tuned by changing the length of the cavity. The filter cavity provides >30 dB of suppression at a detuning of $+\omega_m$ relative to the carrier.

We determine the residual occupation of the microwave mode \bar{n}_e by referring the measured microwave noise spec-

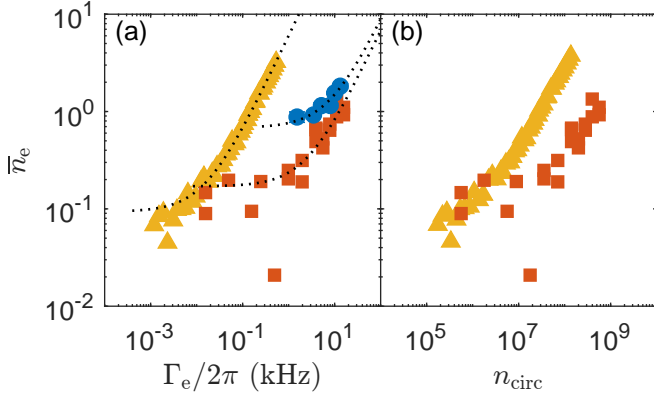


FIG. 4. Microwave effective mode occupancy. (a) \bar{n}_e vs. Γ_e as measured electrically (red squares) and optomechanically (blue circles), compared with electrical measurement of a prior device (yellow triangles) [13]. The dotted lines are linear fits to the data. The Γ_e -dependent noise is reduced by approximately two orders of magnitude relative to the prior device. (b) We represent the electrically measured data as a function of microwave intracavity photon number n_{circ} to account for differences in electromechanical coupling g_e and microwave loss κ_e . We attribute the improvement shown in this representation to a reduction of noise photons generated in the annealed Si_3N_4 film.

tral density $N_{\text{det},e}$ back through the microwave measurement chain and the LC overcoupling ratio, comparing measurements of our current device with similar measurements from a previous device [13] (red squares and yellow triangles, respectively, in Fig. 4(a)). As a consistency check, we also infer \bar{n}_e using sideband asymmetry thermometry of the mechanical mode (blue circles in Fig. 4), optomechanically measured using the optical readout chain, which has higher signal-to-noise ratio than electromechanical measurement in our setup. We fit these data to $\bar{n}_e = a_e \Gamma_e + b_e$ (Table I). Relative to our previous device, we observe the power-dependent term a_e to decrease by approximately two orders of magnitude, enabling a commensurate increase in the transduction bandwidth. We attribute this difference primarily to two internal improvements. The single-photon electromechanical coupling rate g_e in this work increased by approximately 50%. Moreover, the annealed Si_3N_4 film contributed less power-dependent microwave loss and, as we show here, internally generated noise. We disentangle these effects in Fig. 4(b), where we plot \bar{n}_e as a function of the microwave intracavity photon number n_{circ} , related to the previous subfigure by $\Gamma_e = 4g_e^2 n_{\text{circ}} / \kappa_e$. After dividing out the improvements to g_e and power-dependent internal loss κ_e , we find the effective microwave noise is reduced by a factor of five at the highest n_{circ} . The reason we measure a higher value of b_e optomechanically is unknown; we saw no measurable increase in \bar{n}_e as measured from the microwave port when the optical pump was turned on.

TABLE I. Fit to microwave occupancy \bar{n}_e .

device	readout method	$a_e \cdot 2\pi$ (Hz^{-1})	b_e
this work	microwave	$1.05(12) \times 10^{-5}$	0.17(5)
this work	optomechanical	$1.3(2) \times 10^{-5}$	0.7(1)
Ref. [13]	microwave	$9.44(5) \times 10^{-4}$	0.093(6)

Theory of optomechanically stiff modes and the impacts of filtering them out

Whereas the tensile Si_3N_4 membrane is light and has low mechanical dissipation, the thicker and more massive silicon substrate in which it is embedded supports a far denser distribution of lossier and heavier modes. The mechanical modes of the substrate close in frequency to a membrane mode may hybridize with it, usually resulting in a more membrane-mode-like optomechanically compliant mode, and a more substrate-mode-like optomechanically stiff mode. We pattern the substrate into a phononic crystal (PNC) with a periodic structure to reduce coupling between the membrane and substrate modes and reduce the prominence of stiff modes. We designed the PNC so that the center of its bandgap would overlap with the transduction mode at 1.5 MHz.

Due to two simultaneous changes to our transducer design, the PNC was less effective at suppressing stiff modes. First, annealing the Si_3N_4 reduced its tensile stress by $\sim 15\%$ [38], which shifted the transduction mode frequency closer to the band edge. Second, a structural modification accompanying the membrane pinning design affected the performance of the PnC. In addition to the pinning post that defines the ~ 200 nm capacitor spacing between the membrane and the microwave circuit chip, we locate four posts close to the edge of the membrane, along its silicon support frame. These four edge posts perturbed the symmetry of the PNC, reducing its effectiveness at isolating the membrane. The degraded performance of the PnC combined with the shifted mode frequency led to the stiff modes seen in Figs. 1 and 2, and increased γ_m of the transduction mode. We corroborated these hypothesized errors with finite-element simulation and indeed found a higher average density of stiff modes, compared with devices without these five posts. Furthermore, we simulated designs that refine the pinned membrane architecture by relocating the edge posts to places of symmetry with respect to the PnC pattern. These simulations predict a significant reduction of these detrimental effects.

The relatively sharp frequency dependence of the noise spectrum in this device motivates us to define an integrated noise metric that would be relevant for signals taking advantage of the full transduction bandwidth. The minimum noise added to a signal with a given frequency profile can be calculated by computing the overlap integral of the added noise spectrum and normalized sig-

nal. We define the average input-referred added noise in upconversion by integrating over the transduction bandwidth: $\bar{N}_{\text{add}}^{\text{up}} = \int N_{\text{add}}^{\text{up}}(\omega) \cdot \eta(\omega) d\omega / [\int \eta(\omega) d\omega]$.

To recover a weak signal with spectral overlap with the noisy stiff modes, it is possible in principle to notch out the corresponding frequency bands in detection. This would sidestep a very large amount of noise contributed within the bandwidth of the signal, at the cost of a reduction in fidelity of signal due to the portion that is lost, effectively reducing the efficiency of the transducer by an amount η_{filter} . Pitching fast single-photon signals at such a filter would also lead to undesirable ringing, a smearing out of the signals in time, which would be an additional source of inefficiency as well as contribute additional noise to subsequent signals.

To estimate the impact of the drawbacks of implementing a sharp filter at the output of our transducer, we consider a simple protocol of sending single photon signals separated by a repetition time of $t_{\text{rep}} = 3/\Gamma_{\text{T}}$. We consider a Lorentzian with linewidth $\Gamma_{\text{T}}/2\pi = 21.7$ kHz, with the regions indicated by the excluded regions in Fig. 1 (c) removed from the frequency spectrum to create a “notched Lorentzian” frequency profile, and numeri-

cally compute its inverse Fourier transform. Whereas 95% of the transmitted portion of a fast signal filtered through an ideal Lorentzian would be detected within the first t_{rep} of measurement time, 86% of the same signal would be detected in the case of the notched Lorentzian, due to a combination of signal loss from the notched regions of the filter (94% efficiency), as well more of the signal extending beyond t_{rep} from the ringing of the filter (91% efficiency). The latter effect would also contribute on average an additional 0.09 photons/s/Hz of added noise, assuming single photon signals sent at the full repetition rate of this example of once every $t_{\text{rep}} = 3/\Gamma_{\text{T}}$.

Integrating the quantum capacity of a thermal loss channel

Eq. 23 of Ref. [34] gives an upper bound to \mathbf{c} for the bosonic thermal-loss channel, modeled as a beamsplitter of transmissivity η with a thermal state of \bar{n} mean photons. The η of Ref. [34] corresponds to the same η used here, and $\bar{n} = N_{\text{add}} \frac{\eta}{1-\eta}$, which allows us to write Eq. 23 of Ref. [34] as $\mathbf{c} \leq \mathbf{c}_{\text{ub}}$ where

$$\mathbf{c}_{\text{ub}} = \frac{1}{1-\eta} \left(\eta N_{\text{add}} \log_2(N_{\text{add}}) - (1-\eta(1-N_{\text{add}})) \log_2(1-\eta(1-N_{\text{add}})) \right). \quad (6)$$

Since \mathbf{c} is additive for the bosonic thermal-loss channel, we can integrate \mathbf{c}_{ub} over a frequency dependent $\eta(\omega)$ and $N_{\text{add}}(\omega)$ to give us an integrated capacity with a unitful rate dependent on the bandwidth of the channel. Assuming that η has Lorentzian frequency dependence, $\eta(\omega) = \eta \left[1 + \left(\frac{\omega}{2\pi B} \right)^2 \right]^{-1}$, while $N_{\text{add}}(\omega) = N_{\text{add}}$ is constant across frequencies we find that

$$\begin{aligned} \mathcal{C}_{\text{ub}}(N_{\text{add}}, \Theta) = & \frac{2\pi}{\ln(2)} \left[1 - \sqrt{1 - \eta(1 - N_{\text{add}})} \right. \\ & \left. + \frac{\eta N_{\text{add}}}{\sqrt{1 - \eta}} \ln \left(\frac{\sqrt{N_{\text{add}}}(1 + \sqrt{1 - \eta})}{\sqrt{1 - \eta} + \sqrt{1 - \eta(1 - N_{\text{add}})}} \right) \right]. \end{aligned} \quad (7)$$

Taking the limit of Eq. 7 as $\eta \rightarrow 0$ gives Eq. 5, while taking the limit as $\eta \rightarrow 1$ gives $\mathcal{C}_{\text{ub}}(N_{\text{add}}, \Theta) \approx \frac{2\pi\Theta}{\ln(2)} (1 - \sqrt{N_{\text{add}}})$. Thus Eq. 5 underestimates $\mathcal{C}_{\text{ub}}(N_{\text{add}}, \Theta)$ by at most a factor of two.

Transducer performance model

To model our transducer’s noise performance, we use modified versions of Eqs. 1 and 2 that include transducer gain from finite sideband resolution and nonzero internal cavity loss rates $\kappa_{\text{e,int}} = \kappa_{\text{e}} - \kappa_{\text{e,ext}}$ and $\kappa_{\text{o,int}} = \kappa_{\text{o}} -$

$\kappa_{\text{o,ext}}$. Additionally, there is a contribution to \bar{n}_{m} due to the optomechanical backaction of the locking beam used to PDH lock the transducer optical cavity’s resonant frequency $n_{\text{lock}}\gamma_{\text{lock}}$. In downconversion, we have

$$\begin{aligned} N_{\text{add}}^{\text{down}}(\omega_{\text{m}}) = & \frac{n_{\text{th}}\gamma_{\text{m}} + n_{\text{lock}}\gamma_{\text{lock}} + n_{\text{om}}\Gamma_{\text{o}} + n_{\text{em}}\Gamma_{\text{e}}}{\mathcal{A}_{\text{o}}\epsilon^{\frac{\kappa_{\text{o,ext}}}{\kappa_{\text{o}}}}\Gamma_{\text{o}}} \\ & + \frac{\bar{n}_{\text{e}}\kappa_{\text{e,ext}}\Gamma_{\text{T}}^2}{\mathcal{A}\eta_{\text{M}}\kappa_{\text{e}}\Gamma_{\text{e}}\Gamma_{\text{o}}} - \frac{2\bar{n}_{\text{e}}\Gamma_{\text{T}}}{\mathcal{A}_{\text{o}}\epsilon\sqrt{\mathcal{A}_{\text{e}}}\frac{\kappa_{\text{o,ext}}}{\kappa_{\text{o}}}\Gamma_{\text{o}}}. \end{aligned} \quad (8)$$

We use independently calibrated values for $n_{\text{lock}}\gamma_{\text{lock}} = 2\pi \cdot 380$ Hz and $n_{\text{th}}\gamma_{\text{m}} = 2\pi \cdot 4150$ Hz. The expression used for $N_{\text{add}}^{\text{up}}$ is analogous, and only includes the first term as the contribution from \bar{n}_{o} is immeasurably small due to the improvements in our filtering of the optical pump. The microwave circuit occupation $\bar{n}_{\text{e}}(\Gamma_{\text{e}})$ is obtained in downconversion and upconversion from the respective fits in Fig. 4 to the electrically measured and optomechanically inferred values of \bar{n}_{e} .

Operating using a Helium Battery in a cryogen-free dilution refrigerator

We use a BlueFors LD400 dilution refrigerator outfitted with the Helium Battery option to allow us to turn off

the pulse tube for approximately 2 hours of continuous low-vibration measurement time. During this time, the 50 K temperature stage gradually heats up to approximately 100 K, and the resulting thermal expansion causes the optical mode matching factors to change by approximately 20%. To account for this, we periodically measure the mode matching factors, and interpolate these measured values in analyzing our optomechanical measurements. In comparison with the helium precooled dilution refrigerator used in Ref. [13], we observe increased vibration of the optical cavity that we attribute to bubbling of the liquid helium in the battery. This vibration drives a ~ 20 kHz vibrational mode of our optical cavity that the PDH lock to our laser can only partially suppress, resulting in increased optomechanical backaction from the locking beam, due to fast fluctuations of the locking beam detuning.

Microwave readout efficiency calibration

Other than the introduction of the tunable filter cavity, the electromechanical readout chain is comparable to that used in Ref. [13], with the superconducting qubit system and the associated circulator removed, and attenuator values on the microwave input reduced to achieve higher microwave pump powers. Although the prior setup would have similarly enabled measurement of the transducer's downconversion spectrum, the low damping rates used in that work required prohibitively long averaging times to resolve an electromechanical spectrum with similar relative frequency resolution. The orders-of-magnitude greater transduction bandwidths used in this work made such electromechanical measurements tractable in a reasonable amount of time. Whereas the optomechanical readout efficiency can be accurately calibrated using sideband asymmetry thermometry of the compliant mode, this technique is impractical for calibration of the microwave chain due to the difficulty of measuring the cavity-suppressed lower sideband with its lower signal-to-noise ratio. Instead, we take advantage of the high signal-to-noise ratio of the electromechanical signal from the transducer's stiff modes, and the simultaneous optomechanical measurement of that motion. Because the compliant and stiff modes result from hybridization of the same mode with pure membrane motion, the ratio between the optomechanical and electromechanical couplings is identical for these two modes. The microwave readout efficiency can thus be expressed as

$$\xi_e = \xi_o \epsilon_{\text{CL}} \frac{N_{\text{det,e}}(\omega_s)}{N_{\text{det,o}}(\omega_s)} \frac{\kappa_e}{\kappa_{e,\text{ext}}} \frac{\kappa_{o,\text{ext}}}{\kappa_o} \frac{\Gamma_o}{\Gamma_e} \frac{\mathcal{A}_o}{\mathcal{A}_e},$$

where $N_{\text{det,e}}(\omega_s)$ and $N_{\text{det,o}}(\omega_s)$ are the respective electromechanical and optomechanical shot-shot noise normalized spectra at $\omega_s/2\pi = 1.275$ MHz, and are overwhelmingly dominated by motion from the stiff mode at that frequency, and ϵ_{CL} is the factor quantifying the mode matching factor between the transducer's optical cavity and the local oscillator beam used for optical heterodyne detection. This method yields $\xi_e = 0.010(1)$, consistent with an independent measurement of $\xi_e = 0.01$ using measurement of the cryogenic insertion loss of the microwave input lines, and measurement of a signal reflecting promptly from the transducer's microwave resonator with detunings of ± 10 MHz.

Throughput and added noise references

For transducer platforms in upconversion quoted in Fig. 3(c), we use data points from Ref. [12], and include three additional works, summarized in Table II.

TABLE II. Upconversion transducer performances.

Citation	$N_{\text{add}}^{\text{up}}$	η	B (kHz)	D
Higginbotham 2018 [20]	34	0.47	3.5	1
Kumar 2023 [26]	0.6	0.025	360	0.015
Xie 2025 [27]	1.24	0.008	500	2×10^{-4}

For Fig. 3(d), we include two platforms that have reported downconversion performances, summarized in Table III. We make the conservative choice to include optical mode matching efficiency losses for this work, as well as for Refs. [13, 20], as comparable signal losses would be incurred with incorporation into a realistic network. However, we do not include it for other platforms, keeping with the convention used in Ref. [12].

TABLE III. Downconversion transducer performances.

Citation	$N_{\text{add}}^{\text{down}}$	η	B (MHz)	D
Meesala 2024 [11]	0.3	2.4×10^{-4}	1.6	0.008
Sahu 2022 [10]	1.11	0.25	18	3×10^{-7}

Acknowledgments

We thank Terry Brown, Michael Vissers, and John Teufel for technical assistance, and Ravid Shaniv, Benjamin Brubaker, Jonathan Kindem, and Maxwell Olberding for helpful discussions. This work was supported by funding from ARO Grant W911NF2310376, NSF Grant No. PHY-2317149, NSF QLCI Award OMA - 2016244, AFOSR grant FA9550-24-1-0173, NIST, and the Baur-SPIE Endowed Chair at JILA. S.D. additionally thanks support from the DOD through the NDSEG Fellowship Program.